Research Article Vol. 17, No. 11 / 1 Nov 2026 / Biomedical Optics Express 5711
Biomedical Optics EXPRESS

Quantitative photoacoustic tomography for simultaneous reconstruction of optical spectral parameters and speed of sound

MIIKA SUHONEN,[1,*] FELIX LUCKA,[2] AKI PULKKINEN,[1] SIMON ARRIDGE,[3] BEN COX,[4] AND TANJA TARVAINEN[1,3]

[1] University of Eastern Finland, Department of Technical Physics, Kuopio, Finland
[2] Centrum Wiskunde & Informatica, Amsterdam, The Netherlands
[3] University College London, Department of Computer Science, London, United Kingdom
[4] University College London, Department of Medical Physics and Biomedical Engineering, London, United Kingdom
[*] miika.suhonen@uef.fi

Abstract: In this work, we study the inverse problem of quantitative photoacoustic tomography and propose a methodology to simultaneously reconstruct optical spectral parameters and the speed of sound from photoacoustic waves. The developed methodology is based on a coupled forward model, incorporating spectral models representing the wavelength dependence of optical absorption and scattering, a model for light propagation and absorption, and a model for acoustic wave propagation. The inverse problem is solved using a gradient-based algorithm that updates the parameters using an alternating iterative process and utilises multiple different discretisations. Numerical simulations are used to demonstrate that simultaneous reconstruction of optical spectral parameters and the speed of sound in quantitative photoacoustic tomography is feasible when several wavelengths of light and illumination patterns are used. Furthermore, the simulations demonstrate that reference approaches, where either the speed of sound or the scattering parameters are assumed as constants, can produce artefacts in the reconstructed images.

Published by Optica Publishing Group under the terms of the Creative Commons Attribution 4.0 License. Further distribution of this work must maintain attribution to the author(s) and the published article's title, journal citation, and DOI.

1. Introduction

Photoacoustic effect is a physical phenomena in which acoustic pressure waves are created by absorption of a pulsed light. It forms the basis for biomedical imaging modality called quantitative photoacoustic tomography (QPAT) [1–5]. In QPAT, an external excitation of pulsed visible red or near infrared light is used to generate acoustic waves propagating on ultrasound frequencies. These photoacoustic waves are then measured on the boundary of an imaged target using ultrasound sensors. The aim in QPAT is to reconstruct the distributions of the optical parameters of tissue, i.e., absorption and scattering, if one wavelength of light is used, or the concentrations of light absorbing molecules (chromophores) and spectral scattering parameters, if multiple wavelengths are utilised to distinguish spectra of different chromophores. The chromophores of interest are, for example, oxygenated and de-oxygenated hemoglobin.

Conventionally, image reconstruction in QPAT has been considered to consist of two parts, namely acoustic and optical inverse problems. In the acoustic inverse problem, the initial pressure distribution, that has been generated inside the target tissue due to the absorption of optical energy, is reconstructed from measured photoacoustic waves [1,3,6]. The acoustic inverse problem has been studied widely and a large variety of different image reconstruction methods, such as, back propagation, time reversal, analytical methods, regularised least squares methods, a Bayesian approach and deep learning-based approaches have been developed, see e.g. References

#609998 https://doi.org/10.1364/BOE.609998
Journal © 2026 Received 29 Jun 2026; revised 3 Sep 2026; accepted 17 Sep 2026; published 14 Oct 2026

Biomedical Optics EXPRESS

[7–12] and references therein. The optical inverse problem, that is a non-linear, has generally been solved using so-called iterative methods, such as, regularized least squares and Bayesian MAP estimation, see e.g. References [4,5,13–17], and references therein. In addition, so-called direct approaches have been developed [18–22] and, assuming scattering as known, a fixed-point iteration has been applied [23–25]. In addition to two-stage solving of the QPAT inverse problem, single-stage methodologies have been proposed. These are based on merging the optical and acoustic forward models into a single model enabling the optical parameters to be reconstructed directly from the photoacoustic waves [26–35]. Furthermore, reconstruction of quantitative optical parameters values has been applied also *in vivo* [36–38]. These studies, however, utilise a so-called fluence correction rather than modelling the fluence of light while solving the inverse problem.

Generally, to be able to reconstruct both absorption and scattering coefficients uniquely, at least two spatial illumination patterns, that are distinct from each other, are needed [19]. This can be achieved, e.g., using illuminations from different directions [22,39] or spatially modulated illumination patterns [40]. Furthermore, concentrations of chromophores and spectral scattering parameters can be reconstructed if spectral models, that represent the wavelength dependence of absorption and scattering [13,41–43], and data from multiple wavelengths of light are used. In general, using multiple spatial illumination patterns and wavelengths of light can enable simultaneous reconstruction of concentrations of chromophores, wavelength dependent spectral scattering parameters, and the Grüneisen parameter [20,33,44].

When solving the acoustic inverse problem, prior knowledge of the acoustic parameters such as attenuation, speed of sound and acoustic density, are typically considered as known. This not true in general, and thus may lead to artefacts in PAT image reconstruction [45–47]. Especially the speed of sound has a considerable affect on the accuracy of the wave equation and the reconstructed photoacoustic images. To mitigate artefacts due to inaccurate speed of sound in PAT, approaches that utilise ultrasound tomography measurements to estimate the targets speed of sound distribution, that can be then used in photoacoustic tomography image reconstruction, have been developed [48–53]. Furthermore, simultaneous reconstruction of initial pressure and the speed of sound distributions, using only photoacoustic measurements, have been proposed [54–57]. This inverse problem of estimating the speed of sound simultaneously with the initial pressure is highly ill-posed [54,58]. Simultaneous estimation of optical absorption and speed of sound, assuming scattering as known, was considered in Refs. [28,59]. However, to our knowledge, apart from these works, simultaneous reconstruction of optical and acoustic parameters from photoacoustic data alone has not been studied in QPAT. In this work, we propose simultaneous reconstruction of spatially varying optical spectral parameters and the speed of sound in QPAT. As an extension to our previous work on estimation of initial pressure and speed of sound [55], we consider a spectral extension of the model in Ref. [28] enabling reconstruction of concentrations of tissue chromophores, spectral scattering parameters and speed of sound simultaneously. This is enabled by the use of multiple wavelengths of light, spectral models of optical parameters and illuminations from multiple directions.

2. Forward model

In QPAT experiments, a target domain Ω is illuminated with a short near-infrared light pulse. Absorption of light causes an internal temperature rise that leads to pressure increase in the target [3]. This (initial) pressure relaxes as acoustic pressure waves and these propagating waves are measured on the boundary of the target using ultrasound sensors. In the forward problem of QPAT, a model that represents the physical phenomena of light propagation and absorption, photoacoustic effect, and propagation of acoustic waves during the measurement procedure is formed and its solution is numerically approximated.

Biomedical Optics EXPRESS

In a highly scattering medium, the diffusion approximation (DA) of the radiation transfer equation can be used as a light propagation model. The DA combined with a Robin-type boundary condition is of the form

$$\begin{cases} -\nabla \cdot \kappa(r,\lambda)\nabla\Phi(r,\lambda) + \mu_{\mathrm{a}}(r,\lambda)\Phi(r,\lambda) = 0, & r \in \Omega \\ \Phi(r,\lambda) + \frac{1}{2\gamma_d}\kappa(r,\lambda)\frac{\partial\Phi(r,\lambda)}{\partial\hat{n}} = \begin{cases} \mathcal{I}(r,\lambda)\gamma_d^{-1}, & r \in \epsilon \\ 0, & r \notin \epsilon \end{cases} \end{cases} \tag{1}$$

where r is the position, λ is the wavelength, $\Phi(r,\lambda)$ is the photon fluence, $\mu_{\mathrm{a}}(r,\lambda)$ is the absorption coefficient, $\kappa(r,\lambda) = (d(\mu_{\mathrm{a}}(r,\lambda) + \mu_{\mathrm{s}}'(r,\lambda))^{-1}$ is diffusion coefficient, $\mu_{\mathrm{s}}'(r,\lambda)$ is the reduced scattering coefficient and d is the dimension [60,61]. Further, $\mathcal{I}(r,\lambda)$ is the diffuse boundary source at a source position $\epsilon \subset \partial\Omega$, γ_d is a parameter that depends on the dimension ($\gamma_2 = 1/\pi$, $\gamma_3 = 1/4$), and $\hat{n}$ is the outward unit normal. To model the wavelength dependence of the optical parameters, spectral models for absorption and reduced scattering are used

$$\mu_{\mathrm{a}}(r,\lambda) = \sum_{k=1}^{K} \alpha_k(\lambda) C_k(r), \tag{2}$$

$$\mu_{\mathrm{s}}'(r,\lambda) = a(r)\left(\frac{\lambda}{\lambda_{\mathrm{ref}}}\right)^{-b(r)}, \tag{3}$$

where $C_k(r)$, $k = 1,\dots K$ are the concentrations of chromophores that each have distinct absorption spectra described by values $\alpha_k(\lambda)$, $a(r)$ is the reference scattering coefficient at a reference wavelength λ_{ref}, and $b(r)$ is the scattering power [41,44,62].

Optical energy that is absorbed into the tissue chromophores causes an initial acoustic pressure distribution $p_0(r,\lambda)$, that can be calculated as

$$p_0(r,\lambda) = \begin{cases} G(r)\mu_{\mathrm{a}}(r,\lambda)\Phi(r,\lambda), & r \in \Omega \\ 0, & r \notin \Omega \end{cases} \tag{4}$$

where $G(r)$ is Grüneisen parameter describing the photoacoustic efficiency in the target [3]. In this work, it is assumed as a known constant $G(r) = 1$.

In an acoustically non-absorbing medium with constant mass density, the propagation of acoustic waves can be modelled with the acoustic wave equation

$$\left(\frac{1}{c^2(r)}\frac{\partial^2}{\partial t^2} - \nabla^2\right) p(r,\lambda,t) = 0, \quad r \in \mathbb{R}^d,\ t \in (0,T) \tag{5}$$

where $c(r)$ is the speed of sound and $p(r,\lambda,t)$ is the acoustic pressure at a time instance t [3,63,64]. In photoacoustic wave generation, the wave equation is combined with initial conditions

$$p(r,\lambda,0) = p_0(r,\lambda), \quad \frac{\partial}{\partial t}p(r,\lambda,0) = 0. \tag{6}$$

In this work, we approximate the solution of the DA (1) with a finite element method (FEM) [44], using a piecewise linear basis for photon fluence. In addition, the solution of the wave Eq. (5) and (6) is approximated using the k-space pseudo-spectral time-domain method implemented in the k-Wave MATLAB toolbox [65]. The discrete approximation of the coupled forward model is

$$h_j(x) = A_{\mathrm{kW}}\left(\mathrm{diag}\{G\}\mathrm{diag}\{\mu_{\mathrm{a}}\}A_{\mathrm{DA}}^{-1}B_{\mathrm{DA}}\right), \tag{7}$$

where $h_j(x) : \mathbb{R}^{(K+2)N+M} \to \mathbb{R}^{ST}$ is the forward model, j refers to a single light illumination $\mathcal{I}_j$, i.e., one spatial illumination pattern/direction at one wavelength. Further, $x =$

Biomedical Optics EXPRESS

$(C_{1,1}, \ldots, C_{1,N}, \ldots, C_{K,1}, \ldots, C_{K,N}, a_1, \ldots, a_N, b_1, \ldots, b_N, c_1, \ldots, c_M)$ are the target parameters, N is the number of discretisation points of optical spectral parameters, M is the number of discretisation points of speed of sound, S is the number of the sensors and $t = 1, \ldots, T$ denotes the temporal discretisation. Further, $A_{\mathrm{DA}} \in \mathbb{R}^{N\times N}$ and $B_{\mathrm{DA}} \in \mathbb{R}^N$ are the system matrix and source vector of the FE-approximation of the DA, $\mu_{\mathrm{a}} \in \mathbb{R}^N$ is discretised absorption coefficient, $G \in \mathbb{R}^N$ is discretised Grüneisen parameter, $\mathrm{diag}\{\cdot\}$ is a diagonal matrix and A_{kW} is the linear operator approximating the solution of the wave-equation and mapping the solution to data on acoustic sensor locations. In the case of using multiple $j = 1, \ldots, J$ light illuminations, the forward model can be written in the form

$$h(x) = (h_1(x)^\mathsf{T}, \ldots, h_J(x)^\mathsf{T})^\mathsf{T}, \tag{8}$$

where $h(x) : \mathbb{R}^{(K+2)N+M} \to \mathbb{R}^{JST}$.

3. Inverse problem

In this work, we aim to reconstruct concentrations of multiple chromophores, reference scattering, scattering power and the speed of sound. We approach the inverse problem in the Bayesian framework [66,67]. In Bayesian framework, the inverse problem is approached from a statistical point of view and all variables are treated as random variables, with a discrete observation model

$$y = h(x) + e, \tag{9}$$

where $y = \left(y_1^\mathsf{T}, \ldots, y_J^\mathsf{T}\right)^\mathsf{T} \in \mathbb{R}^{JST}$ is data generated by illuminations $j = 1, .., J$ that can consist of different spatial illumination patterns and multiple wavelengths of light. Further, $h(x)$ is the discretised forward model, i.e. Equation (8), $x = (C_1, \ldots, C_K, a, b, c)^\mathsf{T} \in \mathbb{R}^{(K+2)N+M}$ are the target parameters to be reconstructed and $e = \left(e_1^\mathsf{T}, .., e_J^\mathsf{T}\right)^\mathsf{T} \in \mathbb{R}^{JST}$ denotes additive noise. In this work, the optical parameters are presented in a piece-wise linear basis in a triangular (finite element) mesh and speed of sound is presented in a piece-wise constant basis in a pixel (rectangular) mesh. Further, parameters x and noise e are modelled as Gaussian distributed and mutually independent. We solve the *maximum a posteriori* (MAP) estimate by minimising

$$\begin{aligned} x_{\mathrm{MAP}} &= \arg\min_x \left\{ \frac{1}{2} \sum_{j=1}^{J} \left\| L_{e_j} \left(y_j - h_j(x) - \eta_{e_j} \right) \right\|^2 + \frac{1}{2} \left\| L_x (x - \eta_x) \right\|^2 \right\} \\ &= \arg\min_x \{ u(x) \} \end{aligned} \tag{10}$$

where $u(x)$ is the objective function, η_{e_j} is the mean of the noise and $L_{e_j}^\mathsf{T} L_{e_j} = \Gamma_{e_j}^{-1}$ is the Cholesky decomposition, where Γ_{e_j} is the covariance matrix of the noise. Further, η_x is the mean of the prior and $L_x^\mathsf{T} L_x = \Gamma_x^{-1}$, where Γ_x is the covariance matrix of the prior. In practice, the mean η_{e_j} and covariance matrix Γ_{e_j} of the noise can be defined based on the expected noise level of the measurement system. Furthermore, the mean η_x and covariance matrix Γ_x of the prior model can be constructed based on the prior knowledge of the unknown parameters based on using, for example, parameter values that are known from literature for different tissue types. In this work, the Ornstein-Uhlenbeck prior model is used [68], that leads to a block diagonal covariance matrix consisting of covariance matrices for each unknown $\tilde{x}$ of the form

$$\Gamma_{\tilde{x},ij} = \sigma_{\tilde{x}}^2 \exp\left(-\frac{||r_i - r_j||}{\tau_{\tilde{x}}} \right), \tag{11}$$

where $\sigma_{\tilde{x}}$ is the standard deviation, r_i and r_j are the discretisation points, and $\tau_{\tilde{x}}$ is the characteristic length scale describing the spatial smoothness of the parameters and is typically chosen to correspond to the expected size of inclusions in the target.

Biomedical Optics EXPRESS

Minimisation problem (10) can be solved using methods of numerical optimization. In this work, an alternative iterative algorithm presented in Algorithm 1 is used. The algorithm is initialised by using the expected values of the prior model for the unknown parameters as an initial guess. In the alternating approach, only part of the parameters are updated at time, while keeping the others fixed. More specifically, three different sub-problems are considered. In the first sub-problem, concentrations of chromophores are updated while keeping the scattering related parameters and the speed of sound fixed. In the second sub-problem, the speed of sound is updated while the concentration of chromophores and the scattering parameters are kept fixed. In the third sub-problem, the reference scattering and scattering power are updated while keeping the chromophore concentrations and the speed of sound fixed. As concentrations of chromophores act as a source for the photoacoustic signal due to light absorption, it is reasonable to start the iterative process by updating them before other parameter distributions. Furthermore, this order was found to yield the most efficient convergence of the minimisation algorithm. Each sub-problem is solved using the limited memory Broyden–Fletcher–Goldfarb–Shanno (L-BFGS) algorithm with a backtracking line-search [69]. These sub-problems are solved alternately until the entire optimisation problem is converged.

Algorithm 1. Alternating iterative process used to solve minimisation problem (10).

Initialise: $C_1^0, ..., C_K^0, a^0, b^0, c^0, i \leftarrow 0$
for l = Coarsest to finest discretisation **do**
  while Not converged **do**
    $\left(C_1^{i+1}, ..., C_K^{i+1}\right) = \underset{C_1,...,C_K}{\arg\min} \left\{u(C_1^i, ..., C_K^i, a^i, b^i, c^i)\right\}$
    $\left(c^{i+1}\right) = \underset{c}{\arg\min} \left\{u(C_1^{i+1}, ..., C_K^{i+1}, a^i, b^i, c^i)\right\}$
    $\left(a^{i+1}, b^{i+1}\right) = \underset{a,b}{\arg\min} \left\{u(C_1^{i+1}, ..., C_K^{i+1}, a^i, b^i, c^{i+1})\right\}$
    $i \leftarrow i + 1$
  end while
  if $l <$ Finest discretisation **then**
    Change to a discretisation $l + 1$
  end if
end for
Output: $C_{1,\mathrm{MAP}} \leftarrow C_1^i, ..., C_{\mathrm{K,MAP}} \leftarrow C_K^i, a_{\mathrm{MAP}} \leftarrow a^i, b_{\mathrm{MAP}} \leftarrow b^i, c_{\mathrm{MAP}} \leftarrow c^i$

Use of L-BFGS algorithm requires the gradients with respect to objective function to be calculated to find the search direction. In this work, adjoint state method is used to calculate the gradients as follows. The adjoint wave equation is defined as

$$\frac{1}{c^2(r)}\frac{\partial^2}{\partial t^2} q_{\mathrm{a}}(r, \lambda, t) - \nabla^2 q_{\mathrm{a}}(r, \lambda, t) = \Psi(r, \lambda, t), \quad r \in \mathbb{R}^d,\ t \in [0, T], \tag{12}$$

where $q_{\mathrm{a}}(r, \lambda, t)$ is the adjoint pressure wave and $\Psi(r, \lambda, t)$ is the source term of the adjoint equation [70]. Initial conditions for the adjoint wave equation are defined as

$$q_{\mathrm{a}}(r, \lambda, 0) = 0, \quad \frac{\partial}{\partial t} q_{\mathrm{a}}(r, \lambda, 0) = 0. \tag{13}$$

Further, the adjoint equation for the DA can be written as

$$-\nabla \cdot \kappa(r, \lambda)\nabla q_{\mathrm{o}}(r, \lambda) + \mu_{\mathrm{a}}(r, \lambda) q_{\mathrm{o}}(r, \lambda) = q_{\mathrm{a}}(r, \lambda, T) G(r) \mu_{\mathrm{a}}(r, \lambda), \quad r \in \Omega, \tag{14}$$

Biomedical Optics EXPRESS

where $q_{\mathrm{o}}(r,\lambda)$ is the optical adjoint and $q_{\mathrm{a}}(r,\lambda,T)$ is the solution of the (acoustic) adjoint wave equation at a time instance T [30]. The adjoint DA is combined with a boundary condition

$$q_{\mathrm{o}}(r,\lambda)+\frac{1}{2\gamma_d}\kappa(r,\lambda)\frac{\partial q_{\mathrm{o}}(r,\lambda)}{\partial \hat{n}}=0,\quad r\in\partial\Omega. \tag{15}$$

In the discretised setting, with parameters defined similarly as in Sec. 2, the functional gradient for the speed of sound c with respect to the objective functional $u(x)$ (see Eq. (10)) can be written as

$$\frac{\partial u(x)}{\partial c}=\sum_{j=1}^{J}\int_0^T\left(-\frac{2}{c^3}\frac{\partial^2 p_j(r,\lambda,t)}{\partial t^2}\right)^{\mathsf{T}} q_{\mathrm{a},j}(r,\lambda,T-t)\,dt+L_c^{\mathsf{T}}L_c(c-\eta_c) \tag{16}$$

where j refers to a single illumination $\mathcal{I}_j$ [55,71,72]. Furthermore, the functional gradients for the optical spectral parameters can be written as

$$\frac{\partial u(x)}{\partial C_k}=\sum_{j=1}^{J}\alpha_k\frac{\partial u_j(x)}{\partial \mu_{\mathrm{a}}}+L_{C_k}^{\mathsf{T}}L_{C_k}(C_k-\eta_{C_k}) \tag{17}$$

$$\frac{\partial u(x)}{\partial a}=\sum_{j=1}^{J}\left(\frac{\lambda_j}{\lambda_{\mathrm{ref}}}\right)^{-b}\frac{\partial u_j(x)}{\partial \mu_{\mathrm{s}}'}+L_a^{\mathsf{T}}L_a(a-\eta_a) \tag{18}$$

$$\frac{\partial u(x)}{\partial b}=\sum_{j=1}^{J}-a\ln\left(\frac{\lambda_j}{\lambda_{\mathrm{ref}}}\right)\left(\frac{\lambda_j}{\lambda_{\mathrm{ref}}}\right)^{-b}\frac{\partial u_j(x)}{\partial \mu_{\mathrm{s}}'}+L_b^{\mathsf{T}}L_b(b-\eta_b). \tag{19}$$

where the gradients of absorption and scattering with respect to the objective functional are

$$\begin{aligned}\frac{\partial u_j(x)}{\partial \mu_{\mathrm{a}}}&=\left(\frac{\partial A_{\mathrm{DA}}}{\partial \mu_{\mathrm{a}}}\phi_j\right)^{\mathsf{T}} q_{\mathrm{o},j}+\left(\mathrm{diag}\{\phi_j\}\mathrm{diag}\{G\}\right)^{\mathsf{T}} q_{\mathrm{a},j}\\ \frac{\partial u_j(x)}{\partial \mu_{\mathrm{s}}'}&=\left(\frac{\partial A_{\mathrm{DA}}}{\partial \mu_{\mathrm{s}}'}\phi_j\right)^{\mathsf{T}} q_{\mathrm{o},j}.\end{aligned} \tag{20}$$

In the equations above, $q_{\mathrm{o},j}$ is the optical adjoint and $q_{\mathrm{a},j}$ is the acoustic adjoint field at time T. More details about the derivation of the optical parameter gradients can be found, e.g., in Refs. [29,30].

In this work, the parameters are reparametrised to same scale by scaling them with their expected values similary as in [39,73]. Furthermore, when solving the inverse problem, multiple different discretisations are used to avoid the so-called cycle skipping problem [71] and to speed up the calculation process. More precisely, the parameters of interest are first reconstructed in a coarse discretisation, after which the reconstructed parameters are interpolated to a denser discretisation. In this discretisation, the calculation process is continued until convergence. In this work, this is repeated in a total of three different discretisations, and the details of the different discretisations are given later in Sec. 4.2. More information about the benefits of using different discretisations when reconstructing the speed of sound can be found for example in Refs. [55,74].

4. Numerical simulations

The proposed methodology was studied with numerical simulations in full-view and limited-view imaging geometries. In all simulations, a 16 mm × 10 mm rectangular target domain was used. In the full-view simulations, the target was illuminated by four planar illumination patterns, where each pattern covered a single side of the rectangular domain. In the limited-view simulations, the target was illuminated by four planar illumination patterns from top and left sides of the domain,

Biomedical Optics EXPRESS

where each pattern covered half of a single side of the domain. With each illumination pattern, two wavelengths ($\lambda = 750, 850$ nm) of light were used, resulting to a total of 8 illuminations. To simulate acoustic measurements in the full-view imaging geometry, 204 point-like acoustic sensors were placed evenly around the target domain to a distance of a 1 mm from the target boundary. In the limited-view imaging geometry, 102 sensors were placed evenly to a distance of a 1 mm from the target boundary on the top and left sides of the domain. This kind of planar simulation setup mimics a Fabry-Pérot scanner [75–77] with a broad bandwidth and omnidirectional detector response. Illumination patterns and sensor geometries are illustrated in Fig. 1. The proposed approach was used to reconstruct distributions of concentrations of two chromophores, reference scattering, scattering power, and speed of sound.

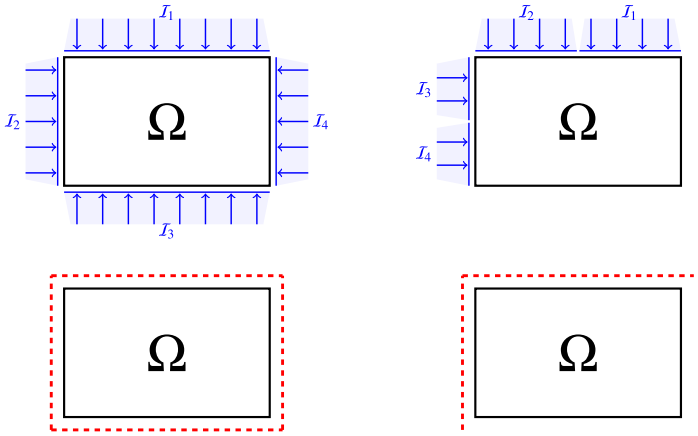


Fig. 1. Illumination patterns and acoustic sensor geometries used in this work in full-view (left column) and limited-view (right column) imaging geometries with a target phantom Ω. Blue arrows illustrate different illumination patterns $\mathcal{I}_1, \ldots, \mathcal{I}_4$ and red dashed line illustrate the locations of acoustic sensors.

In the first set of simulations, the full-view imaging geometry was considered to evaluate the proposed methodology. For reference, reconstructions in a situation where either the speed of sound or scattering parameters were assumed as constant, were calculated. Reference reconstructions were calculated by considering three different cases both for speed of sound and scattering. In the first reference case, a constant value was estimated simultaneously with the unknown spatially varying parameters. In the second reference case, the constant value was fixed to the mean of the prior model. For the third reference case, the constant value was fixed to a some value that was higher than the prior mean.

In the second set of simulations, applicability of the methodology was evaluated both in full-view and limited-view geometries. Furthermore, data simulated using two different noise levels were used.

4.1. Data simulation

In this work, three different numerical phantoms, where optical and acoustic parameters mimicked typical values of soft tissue [41,78–80], were used. The phantoms with their optical and acoustic parameters are illustrated in Fig. 2. The first phantom consisted of simple shapes. The second phantom consisted of a more complex vessel-like structure, and as a third phantom, geometries and parameters of a photoacoustic breast phantom [78] were utilised. The imaged target was modelled to consists of two ($K = 2$) chromophores, namely oxygenated and de-oxygenated hemoglobin. Absorption spectra values for oxygenated and de-oxygenated hemoglobin, see

Biomedical Optics EXPRESS

Eq. (2), that were used in this work, are shown in Table 1 [81]. In the spectral model for scattering, Eq. (3), value $\lambda_{\text{ref}} = 750$ nm was used.

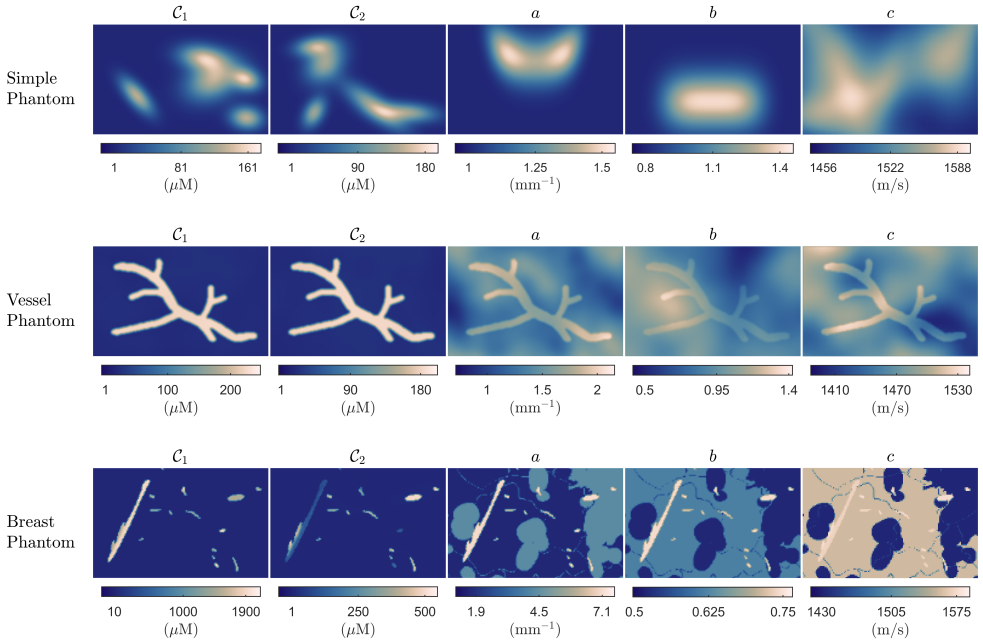


Fig. 2. Concentrations of chromophores C_1 (μM) and C_2 (μM), reference scattering a (mm^{-1}), scattering power b and the speed of sound c (m/s) of the numerical phantoms. Rows from top to bottom: the simple phantom (first row), the vessel phantom (second row), and the breast phantom (third row).

Table 1. Absorption spectra of oxygenated α_1 (M^{-1}mm^{-1}) and de-oxygenated α_2 (M^{-1}mm^{-1}) hemoglobin at different wavelengths of light λ (nm), that were used in the spectral model for the concentrations of chromophores C_1 and C_2, respectively [81].

λ	α_1	α_2
750	355.9	126.5
850	181.0	267.0

To simulate the measurement data, propagation of light was modelled using DA, Eq. (1), and its solution was approximated using FEM, as described in Section 2. In FEM, a discretisation consisting of 25920 triangular elements and 13195 nodes was used. Initial pressure distribution, formed in the target, was modelled as in Eq. (4). Further, propagation of acoustic waves was modelled using acoustic wave Eq. (5) and (6) which solution was numerically approximated using k-space pseudo-spectral time-domain method using the k-Wave toolbox, as described in Section 2. This was carried out using a discretisation that consisted of 13195 pixels, where the center of each pixel corresponded to the location of a FEM node. The calculated initial pressure in the FEM discretisation was interpolated linearly to the discretisation used in the k-Wave. To numerically simulate boundary conditions of the acoustic wave equation, the area was expanded with 10 pixels on each side, where the acoustic point-like sensors were placed, and with a perfectly matched layer (PML) composed of 39 pixels to horizontal (left and right)

Biomedical Optics EXPRESS

sides, and 12 pixels on vertical (bottom and top) sides of the target, to remove reflections on the boundary. The optical and acoustic discretisations are summarised in Table 2. Additive random noise with a zero mean and standard deviation corresponding to the 1% of the peak-to-peak amplitude was added to the simulated photoacoustic data. In addition, a higher noise level of 5% was used in the breast phantom studies. Noisy data simulated in a simple target phantom is presented in Fig. 3.

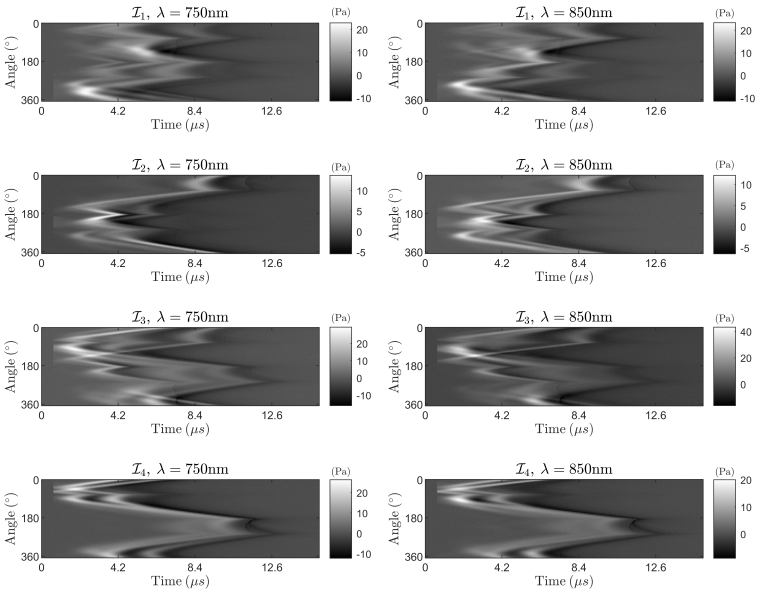


Fig. 3. Sinograms of simulated noisy data using different illumination patterns $\mathcal{I}_1, \ldots, \mathcal{I}_4$ (see Fig. 1), and wavelengths of light λ in a simple target phantom and in a full-view imaging geometry. Angles of the acoustic sensors start from top right corner of the domain (see Fig. 1) and rotate clockwise.

Table 2. Discretisations used in data simulation and in solving of the inverse problem: number of FEM elements N_e and nodes N_n of the optical discretisation, number of pixels in the acoustic discretisation N_p, pixel size ΔN_p (μm), number of pixels placed outside the target domain to place the acoustic sensors to each side N_S, number of pixels added around the computational domain (horizontally and vertically) for the PML N_{PML}, number of time instances N_t, temporal discretisation Δt (ns) and peak supported frequency of the acoustic computation f_p (MHz). Inverse problem discretisations 1.-3. were used for the simple and vessel phantoms, and inverse problem discretisations 2.-4. were used for the breast phantom.

	Data simulation	Inverse problem discretisation 1.	Inverse problem discretisation 2.	Inverse problem discretisation 3.	Inverse problem discretisation 4.
N_e	25920	2880	5120	11520	16048
N_n	13195	1519	2665	5917	8023
N_p	13195	1519	2665	5917	8023
ΔN_p	111	333	250	166	143
N_S	10	4	4	6	8
N_{PML}	39, 12	12, 21	26, 12	13, 26	23, 19
N_t	731	275	322	484	567
Δt	21.2	63.3	47.4	31.6	27.2
f_p	6.4	2.1	2.7	4.0	4.6

Biomedical Optics EXPRESS

4.2. Inverse problem

The minimisation problem (10), was solved using an alternative iterative algorithm (Algorithm 1) as described in Sec. 3. Mean and standard deviation values of the prior model, see Eq. (11), are presented in Table 3 for the three different targets. Characteristic length scale value $\tau_{\tilde{x}} = 2$ mm was used for the simple and vessel-like phantoms. For the breast phantom, $\tau_{\tilde{x}} = 1$ mm was used for the prior models of concentrations of chromophores, and $\tau_{\tilde{x}} = 2$ mm was used for the prior models of scattering parameters and speed of sound. Furthermore, noise of the data was modelled as additive with zero mean and a standard deviation corresponding to a 1% of the peak-to-peak amplitude of the simulated noisy measurement data in all simulations, except in the high noise level simulations using the breast phantom where the noise was modelled as zero mean and standard deviation of 5% peak-to-peak amplitude of the simulated measurement data. As described in Sec. 3, three different discretisations were used in solving the inverse problem, see Table 2.

Table 3. Mean η and standard deviations σ used in the prior modes of concentrations of chromophores C_1 (μM) and C_2 (μM), reference scattering a (mm^{-1}), scattering power b, and speed of sound c (m/s) used in image reconstruction.

	Simple phantom		Vessel-like phantom		Breast phantom	
	η	σ	η	σ	η	σ
C_1	28.8	8.0	50.0	105.4	83.0	317.2
C_2	27.8	9.0	43.0	85.0	13.5	82.7
a	1.08	0.08	1.4	0.20	2.7	0.23
b	0.92	0.10	0.92	0.14	0.60	0.04
c	1524.1	21.9	1465.0	21.6	1515.1	23.7

In addition to visual inspections, the results were evaluated by calculating the relative errors of the reconstructed parameters

$$\mathrm{RE}\ (\%) = 100\% \cdot \frac{||z_{\mathrm{true}} - z_{\mathrm{rec}}||}{||z_{\mathrm{true}} - \min(z_{\mathrm{true}})||}, \tag{21}$$

where z_{true} and z_{rec} are true and reconstructed parameter distributions for each parameter of interest, and offset is removed by subtracting the minimum of the true parameter from the denominator.

4.3. Results

4.3.1. Simple phantom

Reconstructed concentrations of chromophores, reference scattering, scattering power and the speed of sound in a simple target phantom using the full-view imaging geometry are presented in Fig. 4 and the related relative errors are shown in Table 4. As it can be seen, reconstructed concentrations of chromophores resemble the true parameters well as they have similar shapes and the parameter values are close to the true target. Reconstructed reference scattering, scattering power and the speed of sound distributions are noisier than the chromophore reconstructions, but still similar to the true targets. The reconstructed scattering power has lower values in the inclusion compared to the true target distribution. Calculated relative errors for reference scattering, scattering power and speed of sound are higher than the relative errors of concentration of chromophores.

The reference reconstructions where the speed of sound was treated as constant are also shown in Fig. 4 and the corresponding relative errors are given in Table 4. In this case, the reconstructed

Biomedical Optics EXPRESS

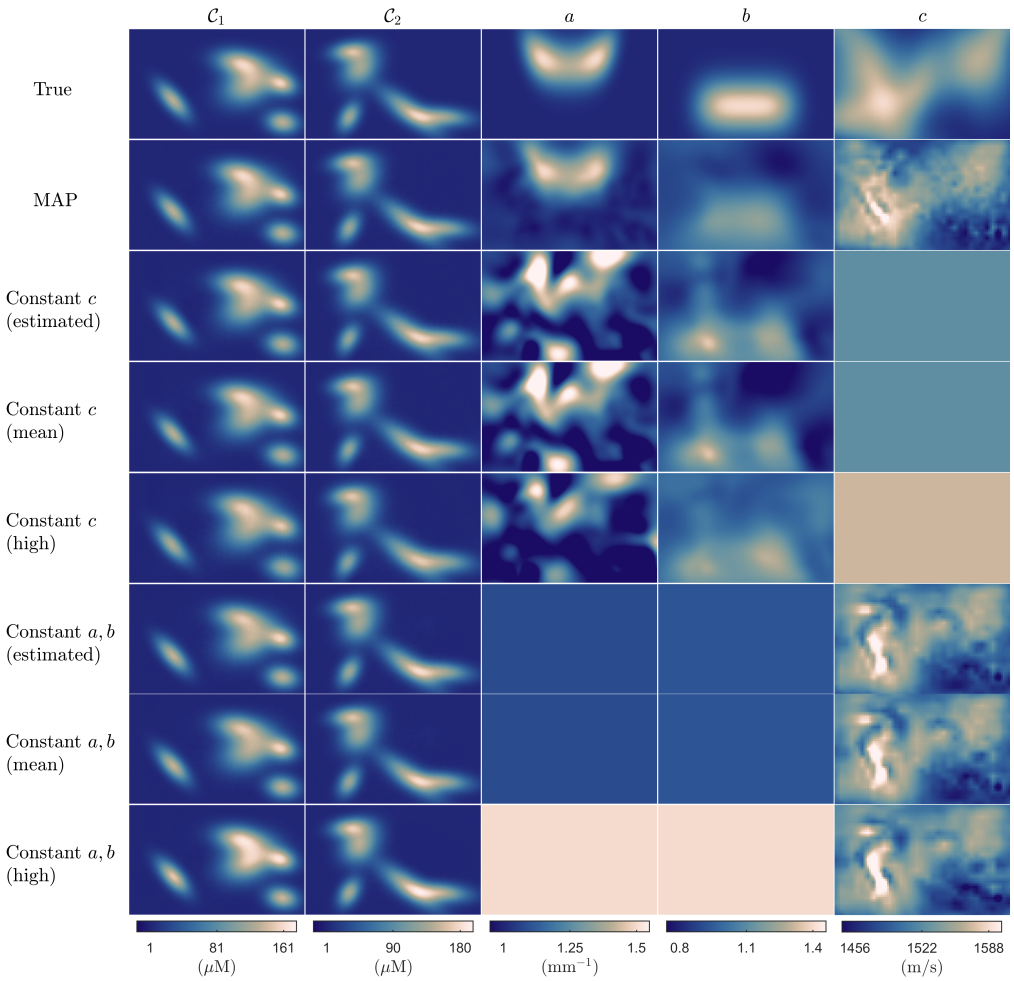


Fig. 4. Concentrations of chromophores $C_1\,(\mu\mathrm{M})$ and $C_2\,(\mu\mathrm{M})$, reference scattering $a\,(\mathrm{mm}^{-1})$, scattering power b and the speed of sound $c\,(\mathrm{m/s})$ in a simple phantom. Rows from top to bottom: true target parameters, MAP estimates using the proposed approach, estimating constant speed of sound, assuming mean value for the constant speed of sound, assuming high constant speed of sound value, estimating constant scattering values, assuming mean values for the constant scattering, assuming high constant scattering values.

concentrations of chromophores resemble the true parameters well. However, the reference scattering and scattering power distributions contain large artefacts, and the inclusions cannot be distinguished. The relative errors in this case are notably higher for all parameters when compared to the proposed approach. Reconstructions, where the constant speed of sound was fixed as the mean of the prior, look similar as in the case of reconstructed constant speed of sound. Further, the relative errors are close to each other. These observations can be expected as the estimated constant speed of sound value is close to the mean of the prior. In the case of constant speed of sound fixed to a higher value, reconstructed chromophores resemble the true targets but the scattering parameters are deformed, similarly as in other reference cases. However, in this case, the relative errors are considerably higher than in other cases for all other parameters, except the reference scattering.

Biomedical Optics EXPRESS

Table 4. Relative errors for concentration of chromophores RE_{C_1} (%) and RE_{C_2} (%), reference scattering RE_a (%), scattering power RE_b (%) and the speed of sound RE_c (%) in the simple and vessel phantoms. Different rows corresponds to: MAP estimates calculated using the proposed approach, estimating constant speed of sound, assuming mean value for the constant speed of sound, assuming high constant speed of sound value, estimating constant scattering values, assuming mean values for the constant scattering, and assuming high constant scattering values. Notation (*) refers to the relative error between the true parameter and the (fixed) constant parameter used in the reconstruction.

		RE_{C_1}	RE_{C_2}	RE_a	RE_b	RE_c
Simple phantom	MAP	1.5	1.8	18.3	43.5	11.1
	Constant c (estimated)	5.5	6.5	99.4	66.7	43.4*
	Constant c (mean)	5.5	6.5	99.9	65.0	43.4*
	Constant c (high)	10.1	9.6	98.1	79.6	75.2*
	Constant a, b (estimated)	4.1	3.4	85.7*	81.5*	19.9
	Constant a, b (mean)	4.1	3.4	85.7*	81.5*	20.3
	Constant a, b (high)	10.9	8.4	278.0*	237.6*	23.9
Vessel phantom	MAP	5.7	7.4	18.1	29.6	16.2
	Constant c (estimated)	17.6	18.1	28.4	42.1	36.5*
	Constant c (mean)	17.8	18.8	27.3	41.7	36.5*
	Constant c (high)	44.8	44.5	60.1	32.2	98.7*
	Constant a, b (estimated)	7.8	7.4	35.4*	36.8*	20.6
	Constant a, b (mean)	7.7	7.4	35.3*	36.8*	20.6
	Constant a, b (high)	24.4	8.1	62.0*	94.9*	23.4

Reference reconstructions and the corresponding relative errors, when a constant scattering was used, are also shown in Fig. 4 and Table 4, respectively. In the reference case where the constant scattering parameters were estimated together with spatially varying chromophores and the speed of sound, concentrations of chromophores resemble the true parameters well. However, the reconstructed speed of sound contains artefacts throughout the domain. In addition, the relative errors are notably higher as those calculated using the proposed approach. When the constant scattering parameters were fixed to the mean of the prior, the reconstructed chromophore concentrations and speed of sound are similar as when the constant scattering parameters were estimated and relative errors are of the same magnitude. The reference where high constant scattering values were used produced reconstructions where the concentrations of chromophores had similar shaped inclusions as in the true parameters but the parameter values in the inclusions were overestimated. This effect can also be noticed from the calculated relative errors that are considerably higher, especially for concentrations of chromophores, than in other cases. Also, the speed of sound suffers from artefacts when high constant scattering is assumed and relative errors are twice as large when compared to the proposed approach.

4.3.2. Vessel phantom

Reconstructions using the proposed approach in a vessel-like target phantom in the full-view imaging geometry are presented in Fig. 5 and the calculated relative errors are shown in Table 4. As it can be seen, the proposed methodology is able to provide reconstructions where the concentrations of chromophores have similar values in the background and in the vessels compared to the true parameter. The reconstructed reference scattering is visually similar as the true target despite the blurriness of the reconstruction. In the reconstruction of the scattering

Biomedical Optics EXPRESS

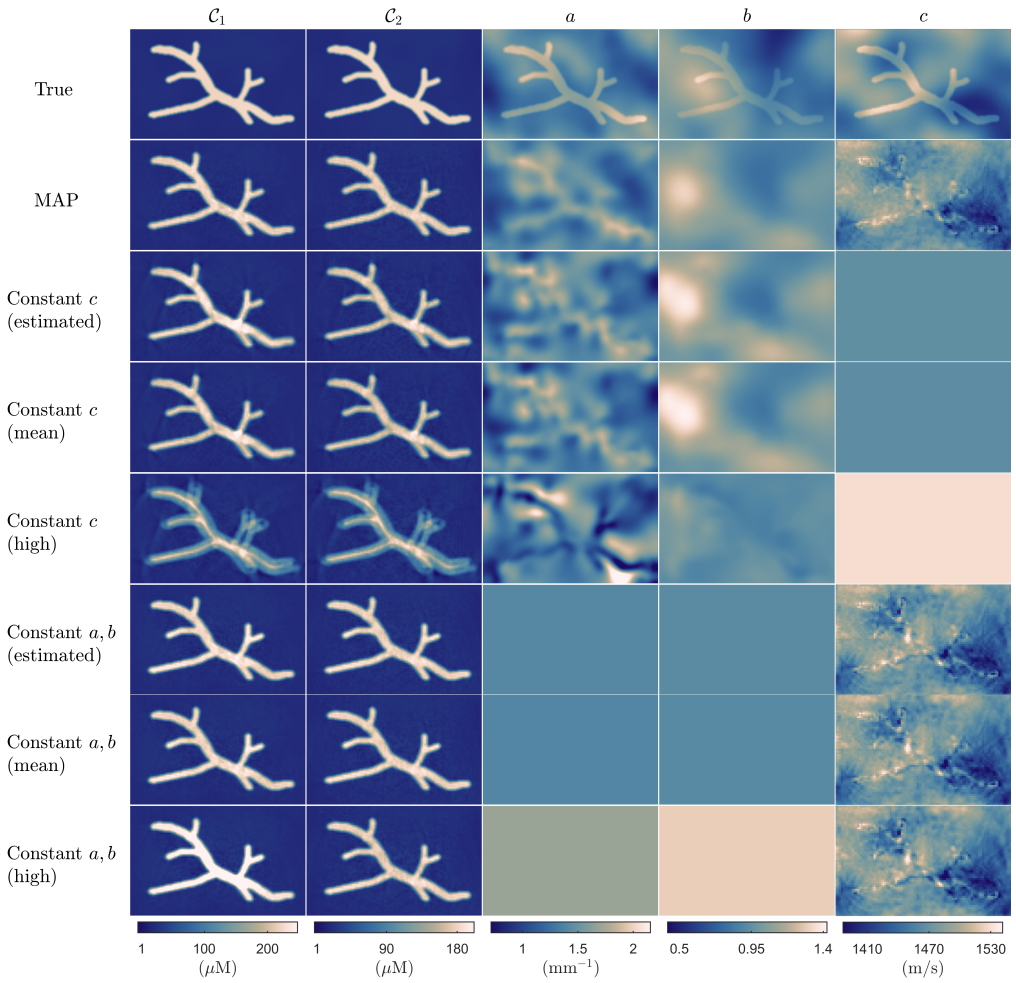


Fig. 5. Concentrations of chromophores $C_1\,(\mu\mathrm{M})$ and $C_2\,(\mu\mathrm{M})$, reference scattering $a\,(\mathrm{mm}^{-1})$, scattering power b and the speed of sound $c\,(\mathrm{m/s})$ in a vessel phantom. Rows from top to bottom: true target parameters, MAP estimates using the proposed approach, estimating constant speed of sound, assuming mean value for the constant speed of sound, assuming high constant speed of sound value, estimating constant scattering values, assuming mean values for the constant scattering, assuming high constant scattering values.

power, the shape of the target can not be detected clearly but regions with high or low values can be seen. The reconstructed speed of sound is distorted but have similar shape and the parameter values are close to the true parameter. Calculated relative errors of concentration of chromophores are notably lower compared to the ones of reference scattering, scattering power and the speed of sound.

The reference reconstructions using a constant speed of sound are also shown in Fig. 5, and the corresponding relative errors are shown in Table 4. The results show that, when a constant speed of sound was estimated simultaneously with spatially varying concentrations of chromophores and scattering parameters, the chromophore reconstructions resemble the true parameters. However, aberrations can be seen on the background of the reconstructions. Reconstruction of reference scattering is distorted and the shape of it is not as clearly detectable as it was when the spatially varying speed of sound was reconstructed. These artefacts in the reconstructions also affect to

Biomedical Optics EXPRESS

the calculated relative errors, that are notably higher compared to the ones calculated using the proposed approach. Similar kind of observations, considering the reconstructions and relative errors, can be seen when the constant speed of sound was set as the mean of the prior. When a high constant speed of sound value was used, reconstructions of chromophores contains high amount of aberrations and the vessel-like structures are not clearly visible. Reconstructed scattering parameters are deformed and does not resemble the true targets. In addition, highest relative errors are found for all other parameters except for scattering power in this case.

Reference reconstructions and the corresponding relative errors, when constant scattering parameters are used, are also shown in Fig. 5 and Table 4, respectively. When estimating constant scattering parameters simultaneously with the chromophore concentrations and speed of sound, or when using the mean of the prior as the constant scattering values, we can see that the reconstructed parameter distributions resemble the true parameters closely, similarly as with the proposed approach. The relative errors are also close to each other in these situations. When using high constant scattering values, the concentrations of chromophores have similar shaped inclusions as in the true parameters but the parameter values in the inclusions of the first concentration of chromophore are notably higher that in the true parameter. Furthermore, similarly as in the other reconstructions, the reconstructed speed of sound is distorted. These observations can also be noticed from the relative errors that are higher than in other constant scattering imaging scenarios.

4.3.3. Breast phantom

Reconstructions using the proposed approach in the breast phantom using both full-view and limited-view imaging geometries as well as 1% and 5% additive noise are shown in Fig. 6. Furthermore, the calculated relative errors are shown in Table 5.

Table 5. Relative errors for concentration of chromophores RE_{C_1} (%) and RE_{C_2} (%), reference scattering RE_a (%), scattering power RE_b (%) and the speed of sound RE_c (%) in the breast phantom. Different rows corresponds to MAP estimates calculated using the proposed approach in: full-view imaging geometry with 1% noise, full-view imaging geometry with 5% noise, limited-view imaging geometry with 1% noise, and limited-view imaging geometry with 5% noise.

	RE_{C_1}	RE_{C_2}	RE_a	RE_b	RE_c
MAP, FV 1%	28.3	80.9	67.9	58.5	28.5
MAP, FV 5%	26.4	80.6	70.0	56.2	24.5
MAP, LV 1%	66.7	91.6	111.5	80.5	69.6
MAP, LV 5%	61.9	92.3	89.1	64.1	58.8

As it can be seen, in the full-view geometry with 1% additive noise in the data, the concentrations of chromophores have similar shapes as the true parameters, but the chromophore C_2 has lower parameter values in the inclusions than the true target. Reconstructed scattering parameters are blurry, and the inclusions cannot be clearly distinguished. The reconstructed speed of sound is distorted but still has parameter values close to the true target values. When looking at the relative errors, it can be seen that the concentration of chromophore C_1 and the speed of sound have lowest relative errors, whereas the relative errors of chromophore C_2 the scattering parameters are high. We suspect that better imaging contrast and lower relative errors could be achieved if the used wavelengths would be chosen more optimally, for example, supporting distinguishability of both chromophores.

In the full-view imaging geometry with 5% noise in the data, the reconstructed parameter distributions resemble the ones calculated in previous case, i.e., with 1% noise in the data.

Biomedical Optics EXPRESS

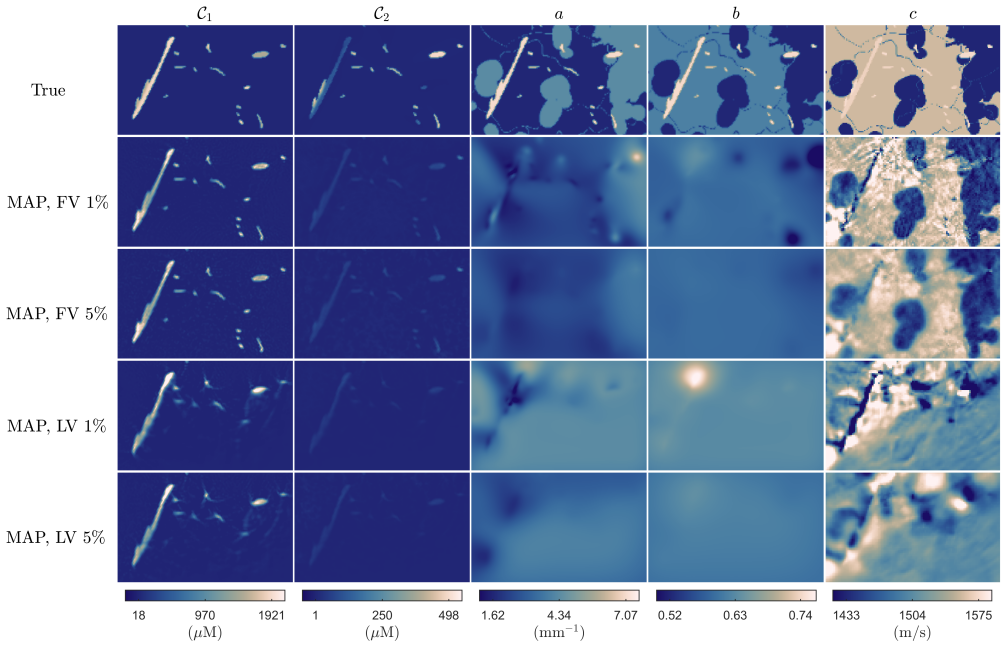


Fig. 6. Concentrations of chromophores $C_1\,(\mu\mathrm{M})$ and $C_2\,(\mu\mathrm{M})$, reference scattering $a\,(\mathrm{mm}^{-1})$, scattering power b and the speed of sound $c\,(\mathrm{m/s})$ in a breast phantom. Rows from top to bottom: true target parameters, MAP estimates using the proposed approach in the full-view imaging geometry with 1% noise, full-view imaging geometry with 5% noise, limited-view imaging geometry with 1% noise, and limited-view imaging geometry with 5% noise.

However, in this case, the concentrations of chromophores show distortion in the background values, and the reconstructed speed of sound is blurry. The calculated relative errors are close to the ones calculated in the case of 1% noise.

In the limited-view imaging situation both with 1% and 5% noise, the inclusions are not distinguishable in the regions of larger distances from the light sources and within the regions that are not enclosed by the acoustic sensors. Furthermore, the relative errors are higher for all parameters compared to the full-view imaging scenarios.

5. Discussion and conclusions

In this work, the inverse problem of quantitative photoacoustic tomography was investigated. A methodology for simultaneous reconstruction of chromophore concentrations, reference scattering, scattering power and the speed of sound was proposed. The developed approach is based on a coupled forward model that models light propagation, photoacoustic effect and acoustic wave propagation, and expresses the optical parameters with their spectral models. The inverse problem was solved using a gradient-based optimisation algorithm that used an alternating iterative process and utilised different discretisations. To ovecome non-uniqueness and alleviate ill-posedness [20,28] multiple illuminations and wavelengths were used.

The proposed approach was studied using numerical simulations. The simulations demonstrated that spatially distributed concentrations of chromophores, reference scattering, scattering power and the speed of sound can be reconstructed simultaneously from photoacoustic waves. We showed that the highest image reconstruction accuracy can be obtained when all parameters of interest are reconstructed simultaneously, compared to situations where the speed of sound or

Biomedical Optics EXPRESS

scattering is assumed as constant in the image reconstruction. Furthermore, assuming these parameters as constant can result in severe reconstruction artefacts if the constant assumption does not match with the true parameter of the target. These results underline the importance of modelling all parameters in QPAT when aim is to reconstruct quantitative values of parameters of interest, for example, concentrations of oxygenated and de-oxygenated hemoglobin.

Overall, reconstructing optical spectral parameters and the speed of sound simultaneously in QPAT is an ill-posed inverse problem, and challenging to solve numerically. In this work, alternating approach for the iterative algorithm, different discretisations and scaling of the parameters were utilised to achieve convergence of the minimisation algorithm. Using these techniques facilitated avoiding local minima that are present due to non-convex nature of the problem. Further, the problem is computationally expensive due to high number of reconstructed parameter distributions, which calls for multiple illumination patterns and wavelengths to be used to remove the non-uniqueness of the problem. For example, on each iteration, J (i.e. total number of illuminations) forward and J adjoint simulations, as well as possible forward simulations needed in the line search, are required. Thus, using multiple light illuminations and a large number of iterations, the total amount of wave simulations needed in the image reconstruction can be substantial. In this work, when using the full-view geometry, the data and solution spaces consisted of $JST = 789888$ data points and $(K+2)N + M = 25895$ unknowns, respectively, in the case of simple and vessel phantoms, and 925344 data points and 40115 unknowns, respectively, in the case of breast phantom. In all simulations, alternating minimisation algorithm converged in less than 1500 iterations with a computational time of ~ 30 h using an Intel Core Ultra 7 – 155H (1.4 GHz) processor. That is, even in this 2D simulation geometry, the computational burden is high, and expanding the methodology to 3D requires efficient methods of scientific computing to be developed and implemented, for example, model reduction methods, methods of parallel computing, and GPU implementations. In addition, the further studies could include optimisation of illumination patterns and wavelengths of light to compress the data without compromising the accuracy of the solution. In addition, using, for example, stochastic optimisation techniques [82] could reduce the computational burden.

In addition to computational aspects, the methodology can be developed further to provide more accurate reconstructions. For example, modelling light propagation using the Monte Carlo method for light transport could enhance the forward model accuracy, e.g., in low scattering regions [83–86]. Furthermore, considering heterogeneous mass density and modelling of acoustic attenuation could provide more accurate forward model for acoustic wave propagation [87]. In addition, possible motion artefacts of the patients, and more accurate modelling of the acoustic sensors, such as frequency responses, need to be considered before clinical translation is possible.

In conclusion, we proposed a methodology for of reconstructing concentrations of two chromophores, reference scattering, scattering power and the speed of sound directly from photoacoustic data in QPAT. The results of this work, that were based on numerical simulations, show that these parameter distributions can be reconstructed simultaneously when multiple illumination patters and several wavelengths of light are used. In addition, as demonstrated with the simulations, constant speed of sound or scattering assumption can cause the reconstructed images to suffer from artefacts.

Funding. European Research Council (101001417 - QUANTOM); Research Council of Finland (353086, 358944); Finnish Cultural Foundation (South Savo Regional Fund); Magnus Ehrnrooth Foundation.

Disclosures. The authors declare no conflicts of interest

Data availability. Data underlying the results presented in this paper are available in Ref. [88].

References

1. P. Beard, "Biomedical photoacoustic imaging," Interface Focus **1**(4), 602–631 (2011).
2. B. Cox, J. Laufer, S. Arridge, *et al.*, "Quantitative spectroscopic photoacoustic imaging: a review," J. Biomed. Opt. **17**(6), 061202 (2012).

Biomedical Optics EXPRESS

3. C. Li and L. Wang, "Photoacoustic tomography and sensing in biomedicine," Phys. Med. Biol. **54**(19), R59–R97 (2009).
4. T. Tarvainen and B. Cox, "Quantitative photoacoustic tomography: modeling and inverse problems," J. Biomed. Opt. **29**(S1), S11509 (2023).
5. Z. Wang, W. Tao, and H. Zhao, "The optical inverse problem in quantitative photoacoustic tomography: A review," Photonics **10**(5), 487 (2023).
6. H. Liu, M. Wang, F. Ji, *et al.*, "Mini review of photoacoustic clinical imaging: a noninvasive tool for disease diagnosis and treatment evaluation," J. Biomed. Opt. **29**(S1), S11522 (2024).
7. X. Deán-Ben and D. Razansky, "A practical guide for model-based reconstruction in optoacoustic imaging," Front. Phys. **10**, 1028258 (2022).
8. A. Hauptmann and B. Cox, "Deep learning in photoacoustic tomography: current approaches and future directions," J. Biomed. Opt. **25**(11), 112903 (2020).
9. P. Kuchment and L. Kunyansky, *Mathematics of Photoacoustic and Thermoacoustic Tomography* (Springer, 2011).
10. J. Poudel, Y. Lou, and M. Anastasio, "A survey of computational frameworks for solving the acoustic inverse problem in three-dimensional photoacoustic computed tomography," Phys. Med. Biol. **64**(14), 14TR01 (2019).
11. A. Rosenthal, V. Ntziachristos, and D. Razansky, "Acoustic inversion in optoacoustic tomography: a review," Curr. Med. Imaging Rev. **9**(4), 318–336 (2013).
12. S. Zhang, J. Miao, and L. Li, "Challenges and advances in two-dimensional photoacoustic computed tomography: a review," J. Biomed. Opt. **29**(07), 070901 (2024).
13. B. Cox, S. Arridge, and P. Beard, "Estimating chromophore distributions from multiwavelength photoacoustic images," J. Opt. Soc. Am. A **26**(2), 443–455 (2009).
14. A. De Cezaro, F. De Cezaro, and J. Suarez, "Regularization approaches for quantitative photoacoustic tomography using the radiative transfer equation," Journal of Mathematical Analysis and Applications **429**(1), 415–438 (2015).
15. W. Naetar and O. Scherzer, "Quantitative photoacoustic tomography with piecewise constant material parameters," SIAM J. Imaging Sci. **7**(3), 1755–1774 (2014).
16. T. Saratoon, T. Tarvainen, B. Cox, *et al.*, "A gradient-based method for quantitative photoacoustic tomography using the radiative transfer equation," Inverse Problems **29**(7), 075006 (2013).
17. T. Tarvainen, A. Pulkkinen, B. Cox, *et al.*, "Bayesian image reconstruction in quantitative photoacoustic tomography," IEEE Trans. Med. Imaging **32**(12), 2287–2298 (2013).
18. B. Banerjee, S. Bagchi, R. Vasu, *et al.*, "Quantitative photoacoustic tomography from boundary pressure measurements: noniterative recovery of optical absorption coefficient from the reconstructed absorbed energy map," J. Opt. Soc. Am. A **25**(9), 2347–2356 (2008).
19. G. Bal and K. Ren, "Multi-source quantitative photoacoustic tomography in a diffusive regime," Inverse Problems **27**(7), 075003 (2011).
20. G. Bal and K. Ren, "On multi-spectral quantitative photoacoustic tomography in diffusive regime," Inverse Problems **28**(2), 025010 (2012).
21. A. Mamonov and K. Ren, "Quantitative photoacoustic imaging in the radiative transport regime," Communications in Mathematical Sciences **12**(2), 201–234 (2014).
22. R. Zemp, "Quantitative photoacoustic tomography with multiple optical sources," Appl. Opt. **49**(18), 3566–3572 (2010).
23. B. Cox, S. Arridge, K. Köstli, *et al.*, "Two-dimensional quantitative photoacoustic image reconstruction of absorption distributions in scattering media by use of a simple iterative method," Appl. Opt. **45**(8), 1866–1875 (2006).
24. T. Harrison, P. Shao, and R. Zemp, "A least-squares fixed-point iterative algorithm for multiple illumination photoacoustic tomography," Biomed. Opt. Express **4**(10), 2224–2230 (2013).
25. T. Jetzfellner, D. Razansky, A. Rosenthal, *et al.*, "Performance of iterative optoacoustic tomography with experimental data," Appl. Phys. Lett. **95**(1), 013703 (2009).
26. M. Bergounioux, T. Haberkorn, and Y. Privat, "An optimal control approach to photoacoustic tomography," in *IEEE 55th Conference Decision Control* pp. 1620–1624 (2016).
27. M. Haltmeier, L. Neumann, and S. Rabanser, "Single-stage reconstruction algorithm for quantitative photoacoustic tomography," Inverse Problems **31**(6), 065005 (2015).
28. T. Ding, K. Ren, and S. Vallélian, "A one-step reconstruction algorithm for quantitative photoacoustic imaging," Inverse Problems **31**(9), 095005 (2015).
29. H. Gao, J. Feng, and L. Song, "Limited-view multi-source quantitative photoacoustic tomography," Inverse Problems **31**(6), 065004 (2015).
30. A. Javaherian and S. Holman, "Direct quantitative photoacoustic tomography for realistic acoustic media," Inverse Problems **35**(8), 084004 (2019).
31. A. Pulkkinen, B. Cox, S. Arridge, *et al.*, "Direct estimation of optical parameters from photoacoustic time series in quantitative photoacoustic tomography," IEEE Trans. Med. Imaging **35**(11), 2497–2508 (2016).
32. P. Shao, T. Harrison, and R. Zemp, "Iterative algorithm for multiple illumination photoacoustic tomography (MIPAT) using ultrasound channel data," Biomed. Opt. Express **3**(12), 3240 (2012).
33. M. Suhonen, A. Pulkkinen, and T. Tarvainen, "Single-stage approach for estimating optical parameters in spectral quantitative photoacoustic tomography," J. Opt. Soc. Am. A **41**(3), 527–542 (2024).

Biomedical Optics EXPRESS

34. N. Song, C. Deumié, and A. Da Silva, "Considering sources and detectors distributions for quantitative photoacoustic tomography," Biomed. Opt. Express **5**(11), 3960–3974 (2014).
35. M. Venugopal, P. van Es, S. Manohar, *et al.*, "Quantitative photoacoustic tomography by stochastic search: direct recovery of the optical absorption field," Opt. Lett. **41**(18), 4202–4205 (2016).
36. Y. Liu, B. Zhang, Y. Ma, *et al.*, "Quantitative photoacoustic imaging algorithm using sparse decomposition for photoacoustic and ultrasound dual-mode imaging," Biomed. Opt. Express **16**(5), 1752–1772 (2025).
37. S. Tzoumas, A. Nunes, I. Olefir, *et al.*, "Eigenspectra optoacoustic tomography achieves quantitative blood oxygenation imaging deep in tissues," Nat. Commun. **7**(1), 12121 (2016).
38. S. Zhang, J. Liu, Z. Liang, *et al.*, "Pixel-wise reconstruction of tissue absorption coefficients in photoacoustic tomography using a non-segmentation iterative method," Photoacoustics **28**, 100390 (2022).
39. T. Tarvainen, B. Cox, J. Kaipio, *et al.*, "Reconstructing absorption and scattering distributions in quantitative photoacoustic tomography," Inverse Problems **28**(8), 084009 (2012).
40. A. Pulkkinen, B. Cox, S. Arridge, *et al.*, "Quantitative photoacoustic tomography using illuminations from a single direction," J. Biomed. Opt. **20**(3), 036015 (2015).
41. S. Jacques, "Optical properties of biological tissues: a review," Phys. Med. Biol. **58**(11), R37–R61 (2013).
42. J. Laufer, B. Cox, E. Zhang, *et al.*, "Quantitative determination of chromophore concentrations from 2D photoacoustic images using a nonlinear model-based inversion scheme," Appl. Opt. **49**(8), 1219–1233 (2010).
43. D. Razansky, M. Distel, C. Vinegoni, *et al.*, "Multispectral opto-acoustic tomography of deep-seated fluorescent proteins *in vivo*," Nat. Photonics **3**(7), 412–417 (2009).
44. A. Pulkkinen, B. Cox, S. Arridge, *et al.*, "A Bayesian approach to spectral quantitative photoacoustic tomography," Inverse Problems **30**(6), 065012 (2014).
45. M. Rietberg, J. Gröhl, T. Else, *et al.*, "Artifacts in photoacoustic imaging: Origins and mitigations," Photoacoustics **45**, 100745 (2025).
46. T. Wang, W. Liu, and C. Tian, "Combating acoustic heterogeneity in photoacoustic computed tomography: A review," J. Innovative Opt. Health Sci. **13**(03), 2030007 (2020).
47. X. Deán-Ben, V. Ntziachristos, and D. Razansky, "Effects of small variations of speed of sound in optoacoustic tomographic imaging," Med. Phys. **41**(7), 073301 (2014).
48. M. Dantuma, F. Lucka, S. Kruitwagen, *et al.*, "Hybrid three-dimensional full-view multi-wavelength photoacoustic and ultrasound breast tomography," Photoacoustics **50**, 100847 (2026).
49. S. Ranjbaran, H. Aghamiry, A. Gholami, *et al.*, "Quantitative photoacoustic tomography using iteratively refined wavefield reconstruction inversion: A simulation study," IEEE Trans. Med. Imaging **43**(2), 874–885 (2024).
50. E. Mercep, J. Herraiz, X. Deán-Ben, *et al.*, "Transmission-reflection optoacoustic ultrasound (TROPUS) computed tomography of small animals," Light: Sci. Appl. **8**(1), 18 (2019).
51. T. Matthews and M. Anastasio, "Joint reconstruction of the initial pressure and speed of sound distributions from combined photoacoustic and ultrasound tomography measurements," Inverse Problems **33**(12), 124002 (2017).
52. M. Segerlund and T. Löfqvist, "A multimodal adjoint-state formulation of quantitative photoacoustic tomography with external acoustic sources," Photoacoustics **51**, 100872 (2026).
53. Y. Zhang and L. Wang, "Adaptive dual-speed ultrasound and photoacoustic computed tomography," Photoacoustics **27**, 100380 (2022).
54. C. Huang, K. Wang, R. Schoonover, *et al.*, "Joint reconstruction of absorbed optical energy density and sound speed distributions in photoacoustic computed tomography: A numerical investigation," IEEE Trans. Comput. Imaging **2**(2), 136–149 (2016).
55. M. Suhonen, F. Lucka, A. Pulkkinen, *et al.*, "Reconstructing multiple initial pressure and speed of sound distributions simultaneously in photoacoustic tomography," Photoacoustics **45**, 100748 (2025).
56. G. Jeong, U. Villa, and M. Anastasio, "Revisiting the joint estimation of initial pressure and speed-of-sound distributions in photoacoustic computed tomography with consideration of canonical object constraints," Photoacoustics **43**, 100700 (2025).
57. A. Kirsch and O. Scherzer, "Simultaneous reconstructions of absorption density and wave speed with photoacoustic measurements," SIAM J. Appl. Math. **72**(5), 1508–1523 (2012).
58. P. Stefanov and G. Uhlmann, "Instability of the linearized problem in multiwave tomography of recovery both the source and the speed," Inverse Problems and Imaging **7**, 1367–1377 (2013).
59. Z. Sun and L. Sun, "Simultaneous reconstruction of optical absorption property and speed of sound in intravascular photoacoustic tomography," Inverse Probl. Sci. Eng. **29**(12), 1764–1788 (2021).
60. S. Arridge, "Optical tomography in medical imaging," Inverse Problems **15**(2), R41–R93 (1999).
61. A. Ishimaru, *Wave Propagation and Scattering in Random Media*, vol. 1 (Academic press, 1978).
62. I. Bigio and S. Fantini, *Quantitative Biomedical Optics: Theory, Methods, and Applications* (Cambridge University Press, 2016).
63. B. Cox, S. Kara, S. Arridge, *et al.*, "*k*-space propagation models for acoustically heterogeneous media: Application to biomedical photoacoustics," J. Acoust. Soc. Am. **121**(6), 3453–3464 (2007).
64. M. Xu and L. Wang, "Photoacoustic imaging in biomedicine," Rev. Sci. Instrum. **77**(4), 041101 (2006).
65. B. Treeby and B. Cox, "k-wave: MATLAB toolbox for the simulation and reconstruction of photoacoustic wave fields," J. Biomed. Opt. **15**(2), 021314 (2010).
66. J. Kaipio and E. Somersalo, *Statistical and Computational Inverse Problems* (Springer, 2005).

Biomedical Optics EXPRESS

67. A. Tarantola, *Inverse Problems Theory and Methods for Model Parameter Estimation* (SIAM, 2005).
68. C. Rasmussen and C. Williams, *Gaussian Processes for Machine Learning* (MIT Press, 2006).
69. J. Nocedal and S. Wright, *Numerical Optimization* (Springer Nature, 2006).
70. S. Arridge, M. Betcke, B. Cox, *et al.*, "On the adjoint operator in photoacoustic tomography," Inverse Problems **32**(11), 115012 (2016).
71. C. Bunks, F. Saleck, S. Zaleski, *et al.*, "Multiscale seismic waveform inversion," Geophysics **60**(5), 1457–1473 (1995).
72. S. Norton, "Iterative inverse scattering algorithms: Methods of computing Fréchet derivatives," J. Acoust. Soc. Am. **106**(5), 2653–2660 (1999).
73. M. Schweiger, S. Arridge, and I. Nissilä, "Gauss-Newton method for image reconstruction in diffuse optical tomography," Phys. Med. Biol. **50**(10), 2365–2386 (2005).
74. F. Lucka, M. Perez-Liva, B. Treeby, *et al.*, "High resolution 3D ultrasonic breast imaging by time-domain full waveform inversion," Inverse Problems **38**(2), 025008 (2022).
75. E. Zhang, J. Laufer, and P. Beard, "Backward-mode multiwavelength photoacoustic scanner using a planar Fabry-Perot polymer film ultrasound sensor for high-resolution three-dimensional imaging of biological tissues," Appl. Opt. **47**(4), 561 (2008).
76. R. Ellwood, O. Ogunlade, E. Zhang, *et al.*, "Photoacoustic tomography using orthogonal Fabry-Pérot sensors," J. Biomed. Opt. **22**(4), 041009 (2017).
77. N. Huynh, E. Zhang, O. Francies, *et al.*, "A fast all-optical 3D photoacoustic scanner for clinical vascular imaging," Nat. Biomed. Eng. **9**(5), 638–655 (2024).
78. S. Park, U. Villa, F. Li, *et al.*, "Stochastic three-dimensional numerical phantoms to enable computational studies in quantitative optoacoustic computed tomography of breast cancer," J. Biomed. Opt. **28**(06), 066002 (2023).
79. J. Sandell and T. Zhu, "A review of in-vivo optical properties of human tissues and its impact on PDT," J. Biophotonics **4**(11-12), 773–787 (2011).
80. T. Szabo, *Diagnostic Ultrasound Imaging: Inside Out (2nd Edition)* (Academic Press, 2014).
81. M. Cope, "The development of a near infrared spectroscopy system and its application for non invasive monitoring of cerebral blood and tissue oxygenation in the newborn infants," Ph.D. thesis, (University College London, 1991).
82. G. Fabien-Ouellet, E. Gloaguen, and B. Giroux, "A stochastic L-BFGS approach for full-waveform inversion," in *SEG Technical Program Expanded Abstracts* pp. 1622–1627 (2017).
83. J. Buchmann, B. Kaplan, S. Powell, *et al.*, "Three-dimensional quantitative photoacoustic tomography using an adjoint radiance Monte Carlo model and gradient descent," J. Biomed. Opt. **24**(06), 1 (2019).
84. R. Hochuli, S. Powell, S. Arridge, *et al.*, "Quantitative photoacoustic tomography using forward and adjoint Monte Carlo models of radiance," J. Biomed. Opt. **21**(12), 126004 (2016).
85. A. Leino, T. Lunttila, M. Mozumder, *et al.*, "Perturbation Monte Carlo method for quantitative photoacoustic tomography," IEEE Trans. Med. Imaging **39**(10), 2985–2995 (2020).
86. N. Hänninen, A. Pulkkinen, S. Arridge, *et al.*, "Adaptive stochastic Gauss-Newton method with optical Monte Carlo for quantitative photoacoustic tomography," J. Biomed. Opt. **27**(08), 083013 (2022).
87. C. Huang, L. Nie, R. Schoonover, *et al.*, "Photoacoustic computed tomography correcting for heterogeneity and attenuation," J. Biomed. Opt. **17**(6), 061211 (2012).
88. M. Suhonen, F. Lucka, A. Pulkkinen, *et al.*, "Quantitative photoacoustic tomography for simultaneous reconstruction of optical spectral parameters and speed of sound: dataset," Zenodo, 2026, https://doi.org/10.5281/zenodo.22247070.